

Bars in low-density environments rotate faster than bars in dense regions

Natalia Puczek,¹ Tobias Géron,^{1,2} Rebecca J. Smethurst¹ and Chris J. Lintott^{1*}

¹*Oxford Astrophysics, Department of Physics, University of Oxford, Denys Wilkinson Building, Keble Road, Oxford OX1 3RH, UK*

²*Dunlap Institute for Astronomy & Astrophysics, University of Toronto, 50 St. George Street, Toronto ON M5S 3H4, Canada*

Accepted XXX. Received YYY; in original form ZZZ

ABSTRACT

Does the environment of a galaxy directly influence the kinematics of its bar? We present observational evidence that bars in high-density environments exhibit significantly slower rotation rates than bars in low-density environments. Galactic bars are central, extended structures composed of stars, dust and gas, present in approximately 30 to 70 per cent of luminous spiral galaxies in the local Universe. Recent simulation studies have suggested that the environment can influence the bar rotation rate, \mathcal{R} , which is used to classify bars as either fast ($1 \leq \mathcal{R} \leq 1.4$) or slow ($\mathcal{R} > 1.4$). We use estimates of \mathcal{R} obtained with the Tremaine–Weinberg method applied to Integral Field Unit spectroscopy from MaNGA and CALIFA. After cross-matching these with the projected neighbour density, $\log \Sigma$, we retain 286 galaxies. The analysis reveals that bars in high-density environments are significantly slower (median $\mathcal{R} = 1.65^{+0.13}_{-0.11}$) compared to bars in low-density environments (median $\mathcal{R} = 1.39^{+0.09}_{-0.08}$); Anderson–Darling p -value of $p_{AD} = 0.002$ (3.1σ). This study marks the first empirical test of the hypothesis that fast bars are formed by global instabilities in isolated galaxies, while slow bars are triggered by tidal interactions in dense environments, in agreement with predictions from numerous N -body simulations. Future studies would benefit from a larger sample of galaxies with reliable Integral Field Unit data, required to measure bar rotation rates. Specifically, more data are necessary to study the environmental influence on bar formation within dense settings (i.e. groups, clusters and filaments).

Key words: galaxies: bar – galaxies: kinematics and dynamics – galaxies : evolution – galaxies: structure – galaxies: statistics – galaxies : formation

1 INTRODUCTION

A bar in a galaxy is a central, extended, long-lived structure composed of stars, dust and gas, present in approximately 30 to 70 per cent of luminous spiral galaxies in the local Universe, with the bar fraction depending on factors such as bar strength, wave-band in which it is observed, galaxy colour and mass (Eskridge et al. 2000; Sheth et al. 2008; Masters et al. 2011; Erwin 2018; Géron et al. 2021). Although *JWST* has now detected bars beyond $z \sim 3$ (a look-back time of 11.5 Gyr; Costantin et al. 2023; Smail et al. 2023; Amvrosiadis et al. 2025; Géron et al. 2025), simulations mark the epoch of bar formation to be around $z \sim 0.7$ –1, coinciding with the galaxies’ transition to being dynamically cool and disc-dominated and a decline in major mergers (Kraljic, Bournaud & Martig 2012; Melvin et al. 2014). In this secular epoch, slow processes become more dominant in galaxy evolution, providing a stable environment for bars to form and persist over long timescales.

Galactic bars are thought to play a critical role in galaxy evolution, funnelling gas to the centre of the galaxy, triggering starbursts and facilitating quenching (Masters et al. 2012; Cheung et al. 2013; Kruk et al. 2018; Géron et al. 2021). Bars allow mass and angular momentum redistribution, stabilizing stellar orbits and influencing subsequent evolution of disc galaxies (Ostriker & Peebles 1973; Combes 2009; Sellwood 2012). Therefore, studying bars is pivotal to building a coherent description of galaxy dynamics.

Both galaxy stellar mass and dark matter halo mass have been suggested as important factors in bar formation and evolution (Fujii et al. 2018; Rosas-Guevara et al. 2020; Kumar, Das & Kataria 2022; Bland-Hawthorn et al. 2023). Although some studies argue that bar formation and evolution are predominantly influenced by the internal processes of the host galaxy (Sarkar, Pandey & Bhattacharjee 2021; Aguerri et al. 2023), the dynamical impact of events such as flybys, minor mergers and satellite interactions on the formation and evolution of barred galaxies has been extensively studied (Kyzliopoulos et al. 2016; Moitazedian et al. 2017; Cavanagh & Bekki 2020; Ghosh et al. 2021). It has long been established that bar formation can be triggered by either tidal interactions (Noguchi 1987; Lang, Holley-Bockelmann & Sinha 2014; Lokas et al. 2016; Gajda, Lokas & Athanassoula 2017; Lokas 2018) or by internal instabilities in cold isolated discs (Hohl 1971; Ostriker & Peebles 1973; Athanassoula, Machado & Rodionov 2013; Sellwood 2014). Simulations further show that tidal interactions can trigger bar formation in galaxies, which would have not otherwise been able to form a bar in isolation (Miwa & Noguchi 1998; Lang et al. 2014; Martinez-Valpuesta et al. 2017). While the internal dynamics and morphologies of hosts are an important factor in the study of bars, bar formation and evolution are also strongly linked to the environment of the galaxy.

However, observational evidence for a relationship between environmental density and bar pattern speed has been lacking. Bar pattern speed, Ω_{bar} , is a fundamental parameter of a bar, as it measures the

* E-mail: cjl@astro.ox.ac.uk (CJL)

angular frequency of the bar's rotation about the galactic centre. Given the variation in galaxy sizes, bar pattern speed is normally parametrised by the bar rotation rate, defined as the dimensionless ratio of the bar's corotation radius, R_{cr} , and its semi-major axis, R_{bar} (Cuomo et al. 2019), that is

$$\mathcal{R} = \frac{R_{\text{cr}}}{R_{\text{bar}}}. \quad (1)$$

The corotation radius is the radius at which the bar and the stars in the disc rotate at the same speed. The bar rotation rate parameter is used to classify bars as either slow ($\mathcal{R} > 1.4$) or fast ($1 \leq \mathcal{R} \leq 1.4$), with the median value of \mathcal{R} being around 1.66 (Géron 2023). Slow bars fall short of R_{cr} , while fast bars extend out to the corotation radius and their pattern speeds are close to the maximum rotation speed allowed at a given bar length. Despite ultrafast bars ($\mathcal{R} < 1$) being unphysical (Contopoulos 1980; Athanassoula 1992), they are repeatedly measured observationally (Rautiainen, Salo & Laurikainen 2008; Font et al. 2017; Guo et al. 2019). This is likely a measurement artefact, as the ultrafast bar phenomenon essentially disappears when bar radius is measured carefully (Roshan et al. 2021; Cuomo et al. 2021). In this paper, we refer to all bars with $\mathcal{R} \leq 1.4$ as fast.

N-body simulations indicate that bars triggered by instabilities within the discs of isolated galaxies are typically fast, whereas bars formed due to tidal interactions are slow (Miwa & Noguchi 1998; Berentzen et al. 2004; Lokas et al. 2014, 2016; Martinez-Valpuesta et al. 2017; Gajda et al. 2017; Lokas 2018). Simulations show that bar evolution in isolated galaxies proceeds through three distinct phases. Once the bar emerges, it continues to grow in the vertical direction for the first ~ 2 Gyr, after which it buckles (bends out of the galactic disc forming a boxy/peanut bulge) becoming shorter and weaker for the next ~ 1 Gyr (Combes & Sanders 1981; Raha et al. 1991; Martinez-Valpuesta & Shlosman 2004). Eventually it enters a phase during which it slows down and gradually grows in length and strength over several Gyr (Raha et al. 1991; Martinez-Valpuesta, Shlosman & Heller 2006; Athanassoula 2013; Sellwood 2014). \mathcal{R} fluctuates across all three stages, but in general, $\mathcal{R} \lesssim 1.4$ for most of the time (Miwa & Noguchi 1998; Berentzen et al. 2004; Martinez-Valpuesta et al. 2017). Simulations of bars influenced or triggered by tidal interactions (i.e. tidal bars) indicate that tidal bars initially undergo weak buckling, after which their rotation rates, \mathcal{R} , decrease gradually for ~ 4 Gyr (Miwa & Noguchi 1998; Martinez-Valpuesta et al. 2017; Gajda et al. 2017; Lokas 2018), such that the bars eventually enter the fast regime, with $\mathcal{R} \sim 1.4$ (Martinez-Valpuesta et al. 2017). None the less, for most of the time, tidal bars are very slow, with $\mathcal{R} \sim 2 - 3$ (Miwa & Noguchi 1998; Berentzen et al. 2004; Lokas et al. 2014, 2016; Gajda et al. 2017; Lokas 2018). Miwa & Noguchi (1998) suggest angular momentum transfer to the perturber as a possible explanation for this slow rotation.

Therefore, \mathcal{R} could be an observational parameter which distinguishes between tidal bars and bars triggered by internal instabilities. Lokas et al. (2016) simulated bar formation on different orbits in a cluster, demonstrating that tidal interactions can trigger or influence bar formation in cluster cores but not in cluster outskirts. Similarly, tidal features in galaxies have been shown to be more frequent in groups and clusters compared to isolated galaxies (Fried 1988). Therefore, we expect that a higher environmental density would lead to a higher fraction of tidal bars. We hypothesise that measurements of bar rotation rate and environmental density should reveal a positive correlation between the two variables. This study is the first observational test of this hypothesis.

To determine whether the simulation results are confirmed by observational data, we use estimates of the rotation rate, \mathcal{R} , obtained for 334 galaxies in the local Universe using the Tremaine–Weinberg method applied to Integral Field Unit (IFU) spectroscopy from Mapping Nearby Galaxies at Apache Point Observatory (MaNGA; Bundy et al. 2015) and Calar Alto Legacy Integral Field Area (CALIFA; Sánchez et al. 2012) surveys, across six studies (Aguerri et al. 2015a; Guo et al. 2019; Cuomo et al. 2019; Garma-Oehmichen et al. 2020, 2022; Géron et al. 2023). We cross-match these with projected neighbour densities, $\log_{10}(\Sigma/\text{Mpc}^{-2})$ (i.e. $\log \Sigma$), from Baldry et al. (2006) using a 10 arcsec search radius, retaining 286 galaxies. To test whether galaxy stellar mass could be responsible for variations in \mathcal{R} , we additionally cross-match the $\log \Sigma$ sample with stellar masses, $\log_{10}(M_{\star}/\text{M}_{\odot})$ (i.e. $\log M_{\star}$), from the MPA-JHU collaboration (Max-Planck Institute for Astrophysics & John Hopkins University; Kauffmann et al. 2003), retaining 275 galaxies. This marks the first empirical test of the assumption that fast bars are formed by global instabilities in the galactic discs of isolated galaxies, while slow bars are triggered by tidal interactions in dense environments.

This paper proceeds as follows: In Section 2 we provide a detailed description of our data sources, galaxy sample and analysis methods. In Section 3 we present the measured relationships between \mathcal{R} , $\log \Sigma$ and $\log M_{\star}$. We discuss the results in Section 4. Finally, we summarise our findings in Section 5.

2 DATA AND METHODS

2.1 Bar rotation rate \mathcal{R} and Tremaine–Weinberg method

We obtain the dimensionless \mathcal{R} measurements for 210 galaxies from Géron et al. (2023), who applied the model-independent kinematic Tremaine–Weinberg (TW) method based on the work of Tremaine & Weinberg (1984) to line-of-sight stellar velocity and stellar flux measurements. The TW method measures the bar pattern speed, Ω_{bar} , by calculating the velocity component misalignment with the major axis of the galaxy. To determine the corotation radius, Géron et al. (2023) combined their measurements of Ω_{bar} with galaxy rotation curves derived from stellar velocity data. For each galaxy, the authors multiplied Ω_{bar} by a range of radii, obtaining a measure of the bar's speed as a function of radius. The radius at which this curve intersected the galaxy rotation curve was the corotation radius. Géron et al. (2023) subsequently combined their measurements of R_{cr} with manual bar length measurements to calculate \mathcal{R} . The authors obtained stellar velocity and stellar flux data from MaNGA IFU in the seventeenth data release of the Sloan Digital Sky Survey (SDSS; Abdurro'uf et al. 2022). Additionally, they made use of Galaxy Zoo DESI (Walmsley et al. 2023) to identify barred galaxies in the IFU survey.

Géron et al. (2023) provide the largest sample of kinematically classified bars to date. However, given the rigorous constraints on data necessary for the TW method, this is still only a small fraction of bars observed by MaNGA. Specifically, the method can only be applied to galaxies with intermediate inclinations ($20^\circ < i < 70^\circ$), since edge-on galaxies do not have accurate spatial measurements, while face-on galaxies lack accurate stellar velocity measurements. Additionally, the bar may not be aligned with the axes of the galaxy, presenting an additional constraint (Tremaine & Weinberg 1984; Géron et al. 2023). As a result, the authors were able to retain only 2 per cent of MaNGA barred galaxies identified by Galaxy Zoo DESI. Therefore, we supplement the galaxy sample with \mathcal{R} measurements from five other studies which also applied the TW method, retaining only the

Table 1. Summary of the bar rotation studies used in our study. The table outlines the IFU spectroscopy catalogue used in the studies and the number of galaxies added to our bar rotation rate, projected neighbour density, and galaxy stellar mass samples.

Study	Catalogue	\mathcal{R}	$\log \Sigma$	$\log M_\star$
Géron et al. (2023)	MaNGA	210	190	185
Garma-Oehmichen et al. (2022)	MaNGA	56	51	46
Garma-Oehmichen et al. (2020)	MaNGA & CALIFA	6	3	3
Cuomo et al. (2019)	CALIFA	16	9	9
Guo et al. (2019)	MaNGA	34	28	27
Aguerri et al. (2015a)	CALIFA	12	5	5
	TOTAL	334	286	275

most recent \mathcal{R} estimate in cases of duplicates, in the same order as they appear in Table 1. This results in a sample containing 334 galaxies with measured \mathcal{R} . Our sample covers the local Universe, with a redshift range $0.017 < z < 0.078$.

2.2 Local environmental density $\log \Sigma$

We use the dimensionless projected neighbour density, $\log_{10} (\Sigma / \text{Mpc}^{-2})$, from Baldry et al. (2006), as a measure of environmental density (measured using spectroscopy from the seventh release of SDSS; Abazajian et al. 2009). The projected neighbour density is available for 286 galaxies from our original sample. $\log \Sigma$ is derived by averaging $\log_{10} (\Sigma_N / \text{Mpc}^{-2})$ for $N = 4$ and 5, where

$$\Sigma_N = \frac{N}{\pi d_N^2}, \quad (2)$$

and d_N [Mpc] is the projected comoving distance to the N^{th} nearest neighbour. A larger (smaller) value of $\log \Sigma$ corresponds to a denser (less dense) environment. The galaxies in our sample have local densities in the range $-1.46 < \log \Sigma < 1.92$. The median measurement uncertainty in our sample is 0.05 dex.

As our sample size is small, with galaxies in the highest-density environments underrepresented, we set cut-offs for the low, intermediate and high-density environments at the 33.3rd and 66.7th percentiles of $\log \Sigma$ (-0.46 and 0.13 , respectively). This approach produces roughly equal-sized density bins. Our low-density bin has a higher cut-off than the $\log \Sigma < -0.8$ cut-off sometimes used to distinguish voids (Baldry et al. 2006; Mouhcine, Baldry & Bamford 2007). However, it aligns with how isolated galaxies are defined by Iovino et al. (2010), who use the $-0.8 < \log \Sigma < -0.4$ range. Bamford et al. (2009) apply an even more generous cut-off of $\log \Sigma < 0$ for low-density environments. Our high-density bin ($\log \Sigma > 0.13$) falls below typical cluster ranges. Mouhcine et al. (2007) use $\log \Sigma > 0.8$ for inner parts of galaxy clusters and Baldry et al. (2006) use $\log \Sigma > 0.8$ for cluster-like environments. It also falls below the lower limit for group environments ($0.4 < \log \Sigma < 0.8$) set by Iovino et al. (2010). Therefore, our low, intermediate and high-density labels refer to relative sample density, with the low-density bin predominantly containing isolated galaxies in void-like regions, and the high-density bin containing a range of dense environments (including groups and clusters).

To test the robustness of our results against the choice of density cut-offs, we repeat the analysis using density cuts shifted to the nearest 0.2 dex relative to the 33.3rd and 66.7th percentiles of $\log \Sigma$ (-0.4 and 0.2). We also explore other subdivisions of $\log \Sigma$ (outlined in

Table 2). We verify that the galaxy stellar mass distributions of the low and high-density subsamples are not statistically distinguishable for each $\log \Sigma$ subdivision (Anderson–Darling p -value $< 1.75 \sigma$). This justifies our decision not to apply mass matching, which would further reduce sample sizes. Such an approach ensures that our results are robust to reasonable variations in sample definition and are unlikely to be driven by sample-selection biases.

2.3 Galaxy stellar mass $\log M_\star$

We use the dimensionless logarithmic median total stellar masses, $\log_{10} (M_\star / M_\odot)$, from the MPA–JHU collaboration (Kauffmann et al. 2003). The authors derived the masses through fits to the seventh release of SDSS photometry (Abazajian et al. 2009). Stellar masses are available for 275 galaxies from the $\log \Sigma$ sample described in the previous paragraph. The galaxies in the $\log \Sigma$ sample have stellar masses in the range $9.38 < \log M_\star < 12.05$. The median measurement uncertainty in our sample is 0.09 dex.

In literature, there are no agreed-upon thresholds for galaxy stellar mass which we could use to separate our sample into low, intermediate and high-mass bins. For example, Sherman et al. (2020) use a $10^{11} M_\odot$ threshold to define high-mass galaxies, while Pérez et al. (2025) use $10^{10.5} M_\odot$ as a cut-off for low-mass and high-mass galaxies. Géron et al. (2021) refer to the $M_\star < 10^{10} M_\odot$ range as low. A reasonable threshold is $M_\star \sim 10^{10.2} M_\odot - 10^{10.3} M_\odot$, which marks a reversal of bar fraction trends in the local Universe (Nair & Abraham 2010; Skibba et al. 2012; Mukundan et al. 2025). However, because of the small sample size in our study, we choose to set the cut-offs at the 33.3rd and 66.7th percentiles of $\log M_\star$, producing roughly equal-sized galaxy stellar mass bins. This corresponds to galaxy stellar masses of $10^{10.51} M_\odot$ and $10^{10.85} M_\odot$, respectively. Therefore, our low-mass bin is consistent with the one used in Pérez et al. (2025), whereas the high-mass cut-off lies between the ones used by Sherman et al. (2020) and Pérez et al. (2025).

2.4 Statistical analysis

To assess the significance of differences between subgroups, we perform the Anderson–Darling test. The null hypothesis is that the values in the low and high-density, or equivalently the low and high-mass subgroups, are drawn from the same population. We require 3σ for statistical significance. We calculate medians of subsamples and their respective uncertainties via bootstrap resampling 5000 times with replacement. We verify that increasing the number of resamples beyond 5000 does not change the inferred medians and confidence intervals. We compute the median for each iteration, and obtain the final median and 1σ uncertainties from the 50th, 16th, and 84th percentiles of the bootstrap distribution.

To account for large asymmetric measurement uncertainties in \mathcal{R} (median individual 1σ measurement uncertainties of -0.37 and $+0.59$), we explicitly propagate them. In each of the 5000 resamples, we perturb the measured values of \mathcal{R} using a distribution constructed from two half-normal distributions joined at the measured value of \mathcal{R} . Such modeling of posterior distributions of \mathcal{R} ensures that we draw values above and below \mathcal{R} with equal probability. In other words, this ensures that the measured values of \mathcal{R} coincide with the medians of the modeled posterior. As such, we sample the downward (upward) perturbations from half-normal distributions with parametrisations set to the reported negative (positive) measurement uncertainties. By construction, this method ensures that the medians and the 16th and 84th percentiles of the modeled posterior distributions coincide with

Table 2. Median values of \mathcal{R} in low, intermediate, and high-density environments (\mathcal{R}_{low} , \mathcal{R}_{mid} and $\mathcal{R}_{\text{high}}$) with 1σ uncertainties for different subdivisions of $\log \Sigma$. N_{low} , N_{mid} and N_{high} are the corresponding sizes of the subgroups. p_{AD} is the Anderson–Darling p -value between the low and high-density subgroups. (1): 33.3rd and 66.7th percentiles, (2): 33.3rd and 66.7th percentiles shifted to the nearest 0.2 dex, (3): 50th percentile, (4): isolated; groups (Iovino et al. 2010), (5): voids; clusters (Baldry et al. 2006; Mouhcine et al. 2007), (6): low-density environments with $\log \Sigma < 0$ (Bamford et al. 2009).

$\log \Sigma$ cut-offs	\mathcal{R}_{low}	N_{low}	\mathcal{R}_{mid}	N_{mid}	$\mathcal{R}_{\text{high}}$	N_{high}	p_{AD}
(1) -0.46 ; 0.13	$1.39^{+0.09}_{-0.08}$	95	$1.52^{+0.11}_{-0.10}$	96	$1.65^{+0.13}_{-0.11}$	95	0.0019 (3.1σ)
(2) -0.4 ; 0.2	$1.40^{+0.09}_{-0.08}$	106	$1.53^{+0.11}_{-0.10}$	97	$1.66^{+0.14}_{-0.12}$	83	0.0028 (3.0σ)
(3) -0.15	$1.40^{+0.08}_{-0.07}$	143	–	–	$1.63^{+0.10}_{-0.09}$	143	0.0032 (2.9σ)
(4) -0.4 ; 0.4	$1.40^{+0.09}_{-0.08}$	106	$1.54^{+0.09}_{-0.09}$	124	$1.71^{+0.20}_{-0.16}$	56	0.0033 (2.9σ)
(5) -0.8 ; 0.8	$1.40^{+0.15}_{-0.12}$	45	$1.52^{+0.07}_{-0.06}$	221	$1.68^{+0.25}_{-0.22}$	20	0.065 (1.8σ)
(6) 0	$1.45^{+0.07}_{-0.07}$	175	–	–	$1.62^{+0.11}_{-0.10}$	111	0.015 (2.4σ)

the measured values of \mathcal{R} and their corresponding lower and upper bounds.

To add a simple measure of the strength of the relationship between \mathcal{R} and $\log \Sigma$, we also calculate the Pearson correlation coefficient, r , along with its p -value, requiring 3σ for statistical significance. While r does not account for measurement uncertainties or intrinsic scatter, it is an easily interpretable metric. As all bars go through multiple phases of evolution, with rotation rates fluctuating across them, we expect substantial scatter in each density bin rather than a tight, one-to-one relation between \mathcal{R} and $\log \Sigma$. To quantify the relationship between the two variables, we use the bivariate correlated errors and intrinsic scatter regression, BCES $y|x$ (Akritas & Bershady 1996). This method accounts for both measurement uncertainties and intrinsic scatter and is a direct extension of the ordinary least-squares approach.

In Section 3, we investigate the dependence of the bar rotation rate on projected neighbour density and galaxy stellar mass by examining the relationship between \mathcal{R} and $\log \Sigma$, as well as comparing the distributions of \mathcal{R} across low and high-density environments and between low and high-mass galaxies. We discuss the results of these tests in Section 4.

3 RESULTS

3.1 Local environmental density $\log \Sigma$

The distributions of \mathcal{R} in the low and high-density subgroups, set by the cut-offs at the 33.3rd and 66.7th percentiles of $\log \Sigma$, are shown in Fig. 1. The median values of \mathcal{R} in the low, intermediate and high-density environments follow a clear positive trend, with $\mathcal{R} = 1.39^{+0.09}_{-0.08}$, $\mathcal{R} = 1.52^{+0.11}_{-0.10}$ and $\mathcal{R} = 1.65^{+0.13}_{-0.11}$, respectively. To assess the significance of the difference between the low-density and high-density environments, we perform the Anderson–Darling test. The null hypothesis is that the \mathcal{R} values in the low and high-density subgroups are drawn from the same population. Both subgroups contain 95 galaxies. We obtain a p -value of $p_{\text{AD}} = 0.002$, which corresponds to a 3.1σ result. Since we require at least 3σ for statistical significance, the Anderson–Darling test indicates that bars hosted in galaxies in low-density environments have significantly lower values of \mathcal{R} (i.e. tend to be faster) than galaxies in high-density environments, despite a big overlap between the two distributions (see Fig. 1).

We repeat the analysis using other subdivisions of $\log \Sigma$ to test the robustness of our results (see Table 2). Shifting the fiducial local density cuts to the nearest 0.2 dex (cut 2) preserves the values of median

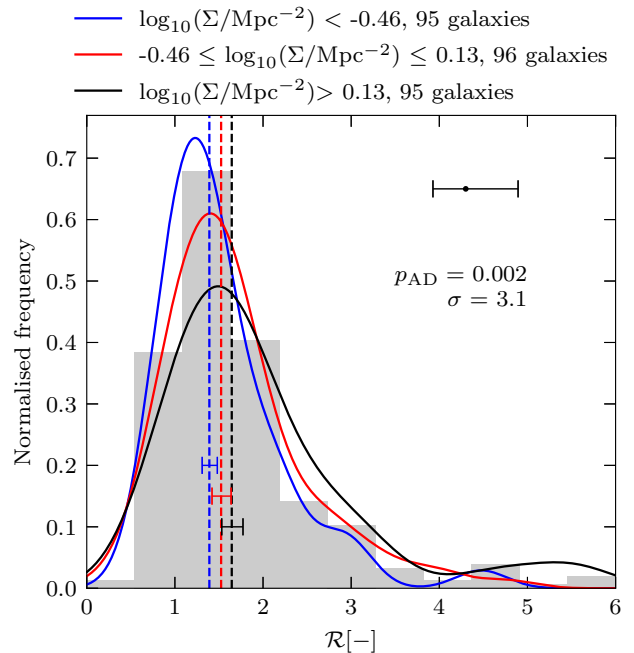


Figure 1. Distributions of the bar rotation rate, \mathcal{R} , for 286 galaxies. The error bar in the top-right corner represents the median measurement uncertainty in \mathcal{R} for individual galaxies. The distributions for the low, intermediate and high-density samples fitted with Gaussian kernel estimates are blue, red and black, respectively. The dashed vertical lines indicate the bootstrapped median values of \mathcal{R} in the samples. The three error bars on the dashed vertical lines represent the bootstrapped asymmetric 1σ uncertainties on the values of median \mathcal{R} in each environment. The Anderson–Darling p -value with the null hypothesis being that the \mathcal{R} values in the low and high-density samples are drawn from the same population is $p_{\text{AD}} = 0.002$, a statistically significant result (3.1σ). This means that galaxies in low-density environments preferentially host faster bars (with lower \mathcal{R}) than galaxies in high-density environments, despite a significant overlap between the two distributions.

\mathcal{R} to within 1%, maintains the positive trend across the low, intermediate and high-density subgroups, and yields a significant Anderson–Darling test ($p_{\text{AD}} = 0.003$, 3.0σ). Using the 50th percentile of $\log \Sigma$ (cut 3) or the $\log \Sigma = -0.4, 0.4$ cuts (cut 4; Iovino et al. 2010) results in slightly lower Anderson–Darling significances (2.9σ), likely due to reduced contrast between subsamples and lower high-density sample size, respectively. None the less, the positive trend in \mathcal{R} and $\log \Sigma$ is maintained. The extreme $\log \Sigma = -0.8, 0.8$ density cuts (cut

5; Baldry et al. 2006; Mouhcine et al. 2007) result in very small sample sizes ($N_{\text{low}} = 45$ and $N_{\text{high}} = 20$) and a nonsignificant Anderson–Darling test ($p_{\text{AD}} = 0.065$, 1.8σ), while using $\log \Sigma = 0$ as a threshold for low/high local densities (cut 6; Bamford et al. 2009) results in moderate Anderson–Darling test significance ($p_{\text{AD}} = 0.015$, 2.4σ). In all cases, median \mathcal{R} consistently show a positive trend with $\log \Sigma$, demonstrating that our results are robust to reasonable variations in the choice of $\log \Sigma$ cut-offs.

Fig. 2 shows a scatter plot between \mathcal{R} and $\log \Sigma$ along with histograms depicting the distributions of both variables. The error bars represent the median measurement errors in \mathcal{R} and $\log \Sigma$ for individual galaxies. We see a weak positive trend between \mathcal{R} and $\log \Sigma$. A robust linear regression accounting for intrinsic scatter, obtained with the BCES $y|x$ method (bivariate correlated errors and intrinsic scatter; Akritas & Bershady 1996), is depicted with the black dashed line. The best-fitting slope between \mathcal{R} and $\log \Sigma$ is $\beta = 0.39 \pm 0.13$ (1σ uncertainty). To better capture the trend in the data, we calculate the Pearson correlation coefficient between \mathcal{R} and $\log \Sigma$ which yields a value of $r = 0.20$ with 3.3σ significance, confirming a statistically significant weakly positive correlation.

3.2 Ultrafast bars $\mathcal{R} < 1$

The fraction of bars with $\mathcal{R} < 1$ in the subgroups with density cut-offs at the 33.3rd and 66.7th percentiles of $\log \Sigma$ decreases with increasing environmental density (19, 16, and 11 per cent from low to high local density), reinforcing the observed trend that bars in denser environments tend to have higher rotation rates. Excluding these bars reduces the significance of the Anderson–Darling test between \mathcal{R} distributions in low and high-density environments from 3.1σ ($p_{\text{AD}} = 0.002$) to 2.7σ ($p_{\text{AD}} = 0.007$). Although this falls slightly below the 3σ required for statistical significance, the trend across the low, intermediate, and high-density subgroups remains consistent, with median \mathcal{R} of $1.54_{-0.10}^{+0.10}$, $1.70_{-0.11}^{+0.12}$ and $1.78_{-0.13}^{+0.15}$, respectively. If we adopt a less strict definition of ultrafast bars, defined as bars which have a 1σ upper limit below $\mathcal{R} = 1$ (Guo et al. 2019; Géron et al. 2023), the ultrafast bar fractions in the low, intermediate and high-density environments drop to 4, 3 and 2 per cent, respectively. The median \mathcal{R} in the environments become $\mathcal{R} = 1.43_{-0.08}^{+0.09}$, $\mathcal{R} = 1.56_{-0.10}^{+0.12}$ and $\mathcal{R} = 1.67_{-0.11}^{+0.13}$, and the Anderson–Darling test gives a statistically significant result, $p_{\text{AD}} = 0.003$ (3.0σ). While ultrafast bars may be measurement artefacts, we discuss in Section 4.2 why we choose not to exclude them from our analysis.

3.3 Galaxy stellar mass $\log M_{\star}$

We next examine whether bar rotation rate depends on galaxy stellar mass. The data in the scatter plot and the histograms in Fig. 2 are coloured based on the 33.3rd and 66.7th percentiles of $\log M_{\star}$. The median values of \mathcal{R} in the low, intermediate and high-mass subgroups are $\mathcal{R} = 1.49_{-0.07}^{+0.07}$, $\mathcal{R} = 1.58_{-0.06}^{+0.06}$ and $\mathcal{R} = 1.40_{-0.07}^{+0.08}$, respectively. To assess the significance of the difference between the low-mass and high-mass environments, we perform the Anderson–Darling test. The null hypothesis is that the \mathcal{R} values in the low and high-mass subgroups are drawn from the same population. We obtain a p -value of $p_{\text{AD}} = 0.17$, which corresponds to 1.4σ , indicating that the distributions do not differ significantly.

The above results suggest that the dynamics of bars depend more strongly on environmental density than on galaxy stellar mass, consistent with theoretical expectations and predictions from simulations.

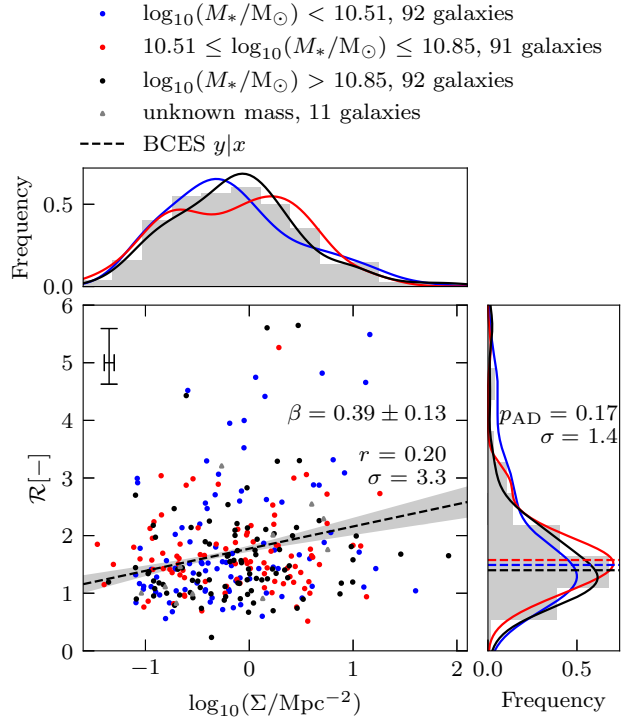


Figure 2. Scatter plot of the bar rotation rate, \mathcal{R} , against projected neighbour density, $\log \Sigma$, for 286 galaxies. The error bars represent the median measurement errors in \mathcal{R} and $\log \Sigma$ for individual galaxies. Low, intermediate and high-mass galaxies are coloured blue, red and black, respectively (the same colouring has been used for the histograms). 11 galaxies with unknown mass are coloured grey. The black dashed line shows a robust linear regression obtained with the BCES $y|x$ method with the grey shaded region representing 1σ confidence. The best-fitting slope to the data obtained with this method is $\beta = 0.39 \pm 0.13$. The Pearson correlation coefficient between \mathcal{R} and $\log \Sigma$ is $r = 0.20$ with 3.3σ significance, indicating a statistically significant weakly positive correlation. The histograms show low, intermediate and high-mass galaxy samples fitted with Gaussian kernel estimates. The Anderson–Darling p -value with the null hypothesis being that the \mathcal{R} values in the low and high-mass samples are drawn from the same population is $p_{\text{AD}} = 0.17$ (1.4σ), so the distributions are not statistically significantly different.

4 DISCUSSION

Studies by Miwa & Noguchi (1998), Berentzen et al. (2004), Lokas et al. (2014, 2016), Martinez-Valpuesta et al. (2017), Gajda et al. (2017) and Lokas (2018) suggest that tidal bars tend to rotate slower with respect to the stellar discs than bars formed by internal disc instabilities, possibly due to angular momentum transfer to the perturber during the interaction, as proposed by Miwa & Noguchi (1998). Since tidal bar formation has been shown to be possible in cluster cores but not in cluster outskirts (Lokas et al. 2016), we hypothesised that a higher environmental density would lead to a higher fraction of tidally triggered bars. Hence, if tidally triggered bars are slower, measurements of \mathcal{R} and $\log \Sigma$ should reveal a positive correlation between the two variables.

4.1 Local environmental density $\log \Sigma$

To test this prediction with observational data, our approach was to compare the bar rotation rates of 286 galaxies across different environmental densities (see Fig. 1). We verified that the galaxy

stellar mass distributions of the low and high-density subsamples are not statistically distinguishable for each $\log \Sigma$ subdivision, justifying our decision not to apply mass matching. We have found that bars in high-density environments are significantly slower than bars in low-density environments ($p_{AD} = 0.002$, 3.1σ). Specifically, in dense environments ($\log \Sigma > 0.13$), we have measured the median $\mathcal{R} = 1.65^{+0.13}_{-0.11}$, whereas in low-density environments ($\log \Sigma < -0.46$), we have measured it to be $\mathcal{R} = 1.39^{+0.09}_{-0.08}$. However, please note the overlap between the distributions in Fig. 1 and the large median individual measurement uncertainty in \mathcal{R} (1σ uncertainties of -0.37 and $+0.59$), which we propagated to estimate the 1σ uncertainties on median \mathcal{R} . A robust linear regression obtained with the BCES $y|x$ method yielded a best-fitting slope of $\beta = 0.39 \pm 0.13$ between \mathcal{R} and $\log \Sigma$ (see Fig. 2). Additionally, we have calculated the Pearson correlation coefficient between \mathcal{R} and $\log \Sigma$ to be $r = 0.20$ with a 3.3σ significance, indicating a statistically significant, albeit weak, positive correlation between \mathcal{R} and $\log \Sigma$.

To test the robustness of our results, we evaluated median \mathcal{R} across low, intermediate and high-density local environments using alternative $\log \Sigma$ cuts (see Table 2). While smaller subsample sizes (cuts 4 and 5) and reduced contrast between subsamples (cuts 3 and 6) naturally decreased the Anderson–Darling test statistical significance, the positive trends between \mathcal{R} and $\log \Sigma$ remained consistent with the trend obtained using the fiducial cuts at the 33.3rd and 66.7th percentiles of $\log \Sigma$.

The Pearson correlation, alongside the outcome of the Anderson–Darling test and the BCES $y|x$ linear regression, is consistent with the scenario in which the rotation rates of bars are influenced by the mechanism behind their formation, with denser environments favouring the formation of slower, tidal bars. This is in support of the predictions from simulations by Miwa & Noguchi (1998), Berentzen et al. (2004), Lokas et al. (2014, 2016), Martinez-Valpuesta et al. (2017), Gajda et al. (2017) and Lokas (2018). It is however important to note that these trends may also reflect variations in bar age or bar slowdown timescales, rather than a direct environmental effect. Zheng & Shen (2025) argue that, when bar strength is taken into account, only galaxies which would not otherwise be able to form bars in isolation develop tidal bars which are slower than internally triggered bars. They propose that the differences in \mathcal{R} are driven by the internal properties of the host galaxies, rather than the bar formation mechanism.

The Tremaine–Weinberg method can only be applied to galaxies which meet strict criteria. Most importantly, the TW method assumes continuity of the tracer (Tremaine & Weinberg 1984). This condition will not be met in a galaxy with a disturbed velocity field due to environmental mechanisms (tidal interactions, ram-pressure stripping, etc.). As a result, galaxies in high-density environments often do not meet the criteria for TW and are discarded in bar studies. This may introduce bias against highly disturbed cluster galaxies and may reduce the sensitivity to the effects of extremely dense environments on bar rotation rates.

As an additional check, we verified that Ω_{bar} , R_{cr} and R_{bar} show no significant correlations with $\log \Sigma$ in the Géron et al. (2023) sample.

4.1.1 The Milky Way bar

Although we did not include the Milky Way (MW) in our statistical analysis, it is instructive to consider the MW’s bar in the context of the observed relationship between \mathcal{R} and $\log \Sigma$. Following the definition of $\log \Sigma$ from Baldry et al. (2006), we approximated the MW’s local environmental density in Appendix A as $\log \Sigma = -0.94$, placing

the MW in a low-density environment. Studies typically place the MW’s bar rotation rate at $\mathcal{R} \sim 1.2$, classifying it as a fast rotator (Portail et al. 2017; Shen & Zheng 2020). Therefore, the MW’s bar rotation rate is qualitatively consistent with the observed tendency for low-density environments to preferentially host faster bars. We note however that \mathcal{R} evolves over time, so the MW’s current bar rotation rate represents only its present evolutionary state, and the above consistency may be coincidental. None the less, the above result suggests that although the MW is atypical in colour-magnitude space (Mutch, Croton & Poole 2011), its bar is not atypical compared to the galaxies in our sample.

4.2 Ultrafast bars $\mathcal{R} < 1$ do not drive the observed trends

In theory, bars which extend beyond R_{cr} should be unstable and rapidly dissolve (Contopoulos 1980; Athanassoula 1992). Despite this, bars with $\mathcal{R} < 1$ are repeatedly measured observationally (Rautiainen et al. 2008; Font et al. 2017; Guo et al. 2019). Although these have been suggested to appear due to overestimated values of R_{bar} (Roshan et al. 2021; Cuomo et al. 2021), the existence of ultrafast bars is widely debated (Aguerri et al. 2015b; Guo et al. 2019; Cuomo et al. 2020; Géron et al. 2023), and we choose not to exclude them from our analysis. The issue requires further investigation and we do not resolve it this paper.

We do however test the robustness of our results to the exclusion of bars with $\mathcal{R} < 1$. Interestingly, we have found that the fraction of bars with $\mathcal{R} < 1$ in the subgroups with $\log \Sigma$ cut-offs at -0.46 and 0.13 decreases with increasing environmental density (19, 16, and 11 per cent from low to high-density local environments), which is consistent with the observed trend that bars in denser environments tend to have higher median \mathcal{R} . Excluding ultrafast bars reduced the significance of the Anderson–Darling test between \mathcal{R} distributions in low and high-density environments from 3.1σ to 2.7σ . Although this falls slightly below 3σ , the trend across the low, intermediate, and high-density subgroups remained consistent (median \mathcal{R} of $1.54^{+0.10}_{-0.10}$, $1.70^{+0.12}_{-0.11}$ and $1.78^{+0.15}_{-0.13}$, respectively), with median \mathcal{R} increasing by ~ 10 per cent in each environment. Adopting a more conservative definition of ultrafast bars, as those with the upper 1σ limit below $\mathcal{R} = 1$ (Guo et al. 2019; Géron et al. 2023), we identified 4, 3 and 2 ultrafast bars in the low, intermediate and high-density environments, respectively. Excluding the ultrafast bars resulted in median \mathcal{R} in the subgroups equal to $\mathcal{R} = 1.43^{+0.09}_{-0.08}$, $\mathcal{R} = 1.56^{+0.12}_{-0.10}$ and $\mathcal{R} = 1.67^{+0.13}_{-0.11}$, respectively, and a statistically significant Anderson–Darling test ($p_{AD} = 0.003$; 3.0σ). The above results suggest that even if the systems which appear to have ultrafast bars are excluded from the analysis, the positive correlation remains. In fact, removing these bars disproportionately reduced the sample size in the low-density bin, which could itself be the source of the decreased Anderson–Darling test significance. While we cannot rule out the possibility that bars with $\mathcal{R} < 1$ arise due to overestimated values of R_{bar} (Roshan et al. 2021; Cuomo et al. 2021), their distribution across local density bins is consistent with the observed positive trend between \mathcal{R} and $\log \Sigma$.

4.3 Galaxy stellar mass $\log M_{\star}$

To test whether galaxy stellar mass could be responsible for variations in \mathcal{R} , we compared the distributions of \mathcal{R} across low, intermediate and high-mass barred galaxies, with their median values of \mathcal{R} being $\mathcal{R} = 1.49^{+0.07}_{-0.07}$, $\mathcal{R} = 1.58^{+0.06}_{-0.06}$ and $\mathcal{R} = 1.40^{+0.08}_{-0.07}$, respectively.

The Anderson–Darling test revealed no significant differences between the distributions of \mathcal{R} in the low and high-mass subgroups ($p_{\text{AD}} = 0.17, 1.4\sigma$; see Fig. 2). It is however important to note the small sample size in this study. This issue could be addressed by increasing the sample size of barred galaxies for which galaxy stellar mass is known and focusing specifically on the relationship between galaxy stellar mass and bar rotation rate. The upcoming Integral Field Unit survey conducted by Hector (Bryant et al. 2020) is of particular interest, as it aims to survey approximately 15,000 galaxies. Assuming that due to the constraints on the TW method only 2 per cent of the data are retained, this would allow to add roughly 300 galaxies to the sample.

5 CONCLUSIONS

We have used the estimates of \mathcal{R} obtained with the Tremaine–Weinberg method applied to IFU spectroscopy from SDSS MaNGA and CALIFA across six studies (Aguerri et al. 2015a; Guo et al. 2019; Cuomo et al. 2019; Garma-Oehmichen et al. 2020, 2022; Géron et al. 2023). Our sample consisted of 334 galaxies in the local Universe ($0.017 < z < 0.078$), which we cross-matched with catalogues containing environmental densities (Baldry et al. 2006) and galactic stellar masses (Kauffmann et al. 2003), marking the first empirical test of the assumption that fast bars are formed by global instabilities in the galaxy disc, while slow bars are triggered or influenced by tidal interactions.

We have found significant evidence consistent with the scenario in which bar rotation rates correlate with formation history, with denser environments preferentially hosting slower bars consistent with tidal formation ($p_{\text{AD}} = 0.002, 3.1\sigma$). Specifically, we have measured the median \mathcal{R} in low ($\log \Sigma < -0.46$) and high-density ($\log \Sigma > 0.13$) environments to be $\mathcal{R} = 1.39^{+0.09}_{-0.08}$ and $\mathcal{R} = 1.65^{+0.13}_{-0.11}$, respectively. Although the correlation between \mathcal{R} and $\log \Sigma$ was statistically significant, its strength was modest ($r = 0.2; 3.3\sigma$), indicating a subtle environmental dependence. We subsequently tested the robustness of our results against different density cut-offs. Although all subdivisions led to reduced Anderson–Darling test significance, the positive trend between \mathcal{R} and $\log \Sigma$ remained consistent with our hypothesis. Additionally, we have found no evidence suggesting significant differences in the bar pattern speed between low and high-mass galaxies.

These results will be solidified by new Integral Field Unit data. An exciting upcoming survey will be conducted by Hector, a spectrograph installed on the Anglo-Australian Telescope. Hector aims to survey approximately 15,000 galaxies up to 2 effective radii (Bryant et al. 2020). This extensive survey will significantly increase the number of galaxies to which the Tremaine–Weinberg method can be applied, adding roughly 300 galaxies to the sample in this paper. We encourage observations of barred galaxies with IFUs as a means of providing insight into their formation and evolution.

ACKNOWLEDGEMENTS

We thank the referee for the interesting idea to investigate whether the Milky Way bar follows the observed relationship between \mathcal{R} and environment. We also thank Yirui Zheng for the helpful discussion on tidal bars, and Marcin Semczuk for suggesting that we comment on the correlation between $\log \Sigma$ and Ω_{bar} , R_{cr} and R_{bar} .

DATA AVAILABILITY

This research has made use of publicly available data. The \mathcal{R} data were obtained from six independent sources: Géron et al. (2023) (<https://zenodo.org/records/7567945>), Garma-Oehmichen et al. (2022) (https://github.com/lgarma/MWA_pattern_speed), Garma-Oehmichen et al. (2020, Table 4), Guo et al. (2019, Table 4) (values taken from column \mathcal{R}_1), Cuomo et al. (2019, Table 2) and Aguerri et al. (2015a, Table 4) (values taken from column \mathcal{R}_1). Measurements of stellar masses ($\log M_{\star}$) and neighbour density ($\log \Sigma$) were taken from publicly available catalogues cited in the text. The Catalog & Atlas of the LV galaxies (Karachentsev et al. 2013) was used to obtain an estimate of $\log \Sigma$ for the Milky Way (Appendix A).

REFERENCES

Abazajian K. N., et al., 2009, *ApJS*, **182**, 543
 Abdurro'uf et al., 2022, *ApJS*, **259**, 35
 Aguerri J. A. L., et al., 2015a, *A&A*, **576**, A102
 Aguerri J. A. L., et al., 2015b, *A&A*, **576**, A102
 Aguerri J. A. L., Cuomo V., Rojas-Roncero A., Morelli L., 2023, *A&A*, **679**, A5
 Akitas M. G., Bershady M. A., 1996, *ApJ*, **470**, 706
 Amvrosiadis A., et al., 2025, *MNRAS*, **537**, 1163
 Athanassoula E., 1992, *MNRAS*, **259**, 345
 Athanassoula E., 2013, in Falcón-Barroso J., Knapen J. H., eds, , Secular Evolution of Galaxies. Proceedings of the XXIII Canary Islands Winter School of Astrophysics. Cambridge Univ. Press, Cambridge, p. 305
 Athanassoula E., Machado R. E. G., Rodionov S. A., 2013, *MNRAS*, **429**, 1949
 Baldry I. K., Balogh M. L., Bower R. G., Glazebrook K., Nichol R. C., Bamford S. P., Budavari T., 2006, *MNRAS*, **373**, 469
 Bamford S. P., et al., 2009, *MNRAS*, **393**, 1324
 Berentzen I., Athanassoula E., Heller C. H., Fricke K. J., 2004, *MNRAS*, **347**, 220
 Bland-Hawthorn J., Tepper-Garcia T., Agertz O., Freeman K., 2023, *ApJ*, **947**, 80
 Bryant J. J., et al., 2020, in Evans C. J., Bryant J. J., Motohara K., eds, Proc. SPIE Conf. Ser. Vol. 11447, Ground-based and Airborne Instrumentation for Astronomy VIII. SPIE, Bellingham, p. 1144715
 Bundy K., et al., 2015, *ApJ*, **798**, 7
 Cavanagh M. K., Bekki K., 2020, *A&A*, **641**, A77
 Cheung E., et al., 2013, *ApJ*, **779**, 162
 Combes F., 2009, in Jogeé S., Marinova I., Hao L., Blanc G. A., eds, ASP Conference Series Vol. 419, Active Galaxies. Galaxy Evolution: Emerging Insights and Future Challenges. Astron. Soc. Pac., San Francisco, p. 31
 Combes F., Sanders R. H., 1981, *A&A*, **96**, 164
 Contopoulos G., 1980, *A&A*, **81**, 198
 Costantin L., et al., 2023, *Nature*, **623**, 499
 Cuomo V., Lopez Aguerri J. A., Corsini E. M., Debattista V. P., Méndez-Abreu J., Pizzella A., 2019, *A&A*, **632**, A51
 Cuomo V., Aguerri J. A. L., Corsini E. M., Debattista V. P., 2020, *A&A*, **641**, A111
 Cuomo V., Lee Y. H., Buttitta C., Aguerri J. A. L., Corsini E. M., Morelli L., 2021, *A&A*, **649**, A30
 Erwin P., 2018, *MNRAS*, **474**, 5372
 Eskridge P. B., et al., 2000, *AJ*, **119**, 536
 Font J., et al., 2017, *ApJ*, **835**, 279
 Fried J. W., 1988, *A&A*, **189**, 42
 Fujii M. S., Bédorf J., Baba J., Portegies Zwart S., 2018, *MNRAS*, **477**, 1451
 Gajda G., Łokas E. L., Athanassoula E., 2017, *ApJ*, **842**, 56
 Garma-Oehmichen L., Cano-Díaz M., Hernández-Toledo H., Aquino-Ortíz E., Valenzuela O., Aguerri J. A. L., Sánchez S. F., Merrifield M., 2020, *MNRAS*, **491**, 3655

Garma-Oehmichen L., et al., 2022, *MNRAS*, **517**, 5660
 Géron T., 2023, PhD thesis, University of Oxford
 Géron T., Smethurst R. J., Lintott C., Kruk S., Masters K. L., Simmons B., Stark D. V., 2021, *MNRAS*, **507**, 4389
 Géron T., et al., 2023, *MNRAS*, **521**, 1775
 Géron T., et al., 2025, *ApJ*, **987**, 74
 Ghosh S., Saha K., Di Matteo P., Combes F., 2021, *MNRAS*, **502**, 3085
 Guo R., Mao S., Athanassoula E., Li H., Ge J., Long R. J., Merrifield M., Masters K., 2019, *MNRAS*, **482**, 1733
 Hohl F., 1971, *ApJ*, **168**, 343
 Iovino A., et al., 2010, *A&A*, **509**, A40
 Karachentsev I. D., Makarov D. I., Kaisina E. I., 2013, *AJ*, **145**, 101
 Kauffmann G., et al., 2003, *MNRAS*, **341**, 33
 Kraljic K., Bournaud F., Martig M., 2012, *ApJ*, **757**, 60
 Kruk S. J., et al., 2018, *MNRAS*, **473**, 4731
 Kumar A., Das M., Kataria S. K., 2022, *MNRAS*, **509**, 1262
 Kyzliopoulos P. E., Eftymiopoulos C., Gravvanis G. A., Patsis P. A., 2016, *MNRAS*, **463**, 2210
 Lang M., Holley-Bockelmann K., Sinha M., 2014, *ApJ*, **790**, L33
 Łokas E. L., 2018, *ApJ*, **857**, 6
 Łokas E. L., Athanassoula E., Debattista V. P., Valluri M., Pino A. d., Semczuk M., Gajda G., Kowalczyk K., 2014, *MNRAS*, **445**, 1339
 Łokas E. L., Ebróvá I., del Pino A., Sybilska A., Athanassoula E., Semczuk M., Gajda G., Fouquet S., 2016, *ApJ*, **826**, 227
 Martinez-Valpuesta I., Shlosman I., 2004, *ApJ*, **613**, L29
 Martinez-Valpuesta I., Shlosman I., Heller C., 2006, *ApJ*, **637**, 214
 Martinez-Valpuesta I., Aguerrí J. A. L., González-García A. C., Dalla Vecchia C., Stringer M., 2017, *MNRAS*, **464**, 1502
 Masters K. L., et al., 2011, *MNRAS*, **411**, 2026
 Masters K. L., et al., 2012, *MNRAS*, **424**, 2180
 Melvin T., et al., 2014, *MNRAS*, **438**, 2882
 Miwa T., Noguchi M., 1998, *ApJ*, **499**, 149
 Moetazedian R., Polyachenko E. V., Berczik P., Just A., 2017, *A&A*, **604**, A75
 Mouhcine M., Baldry I. K., Bamford S. P., 2007, *MNRAS*, **382**, 801
 Mukundan K., Nair P., Masters K. L., Bailin J., Gwartney P., Li W., 2025, *MNRAS*, **542**, 151
 Mutch S. J., Croton D. J., Poole G. B., 2011, *ApJ*, **736**, 84
 Nair P. B., Abraham R. G., 2010, *ApJ*, **714**, L260
 Noguchi M., 1987, *MNRAS*, **228**, 635
 Ostriker J. P., Peebles P. J. E., 1973, *ApJ*, **186**, 467
 Pérez I., et al., 2025, *A&A*, **695**, A84
 Portail M., Gerhard O., Wegg C., Ness M., 2017, *MNRAS*, **465**, 1621
 Raha N., Sellwood J. A., James R. A., Kahn F. D., 1991, *Nature*, **352**, 411
 Rautiainen P., Salo H., Laurikainen E., 2008, *MNRAS*, **388**, 1803
 Rosas-Guevara Y., et al., 2020, *MNRAS*, **491**, 2547
 Roshan M., Banik I., Ghafourian N., Thies I., Famaey B., Asencio E., Kroupa P., 2021, *MNRAS*, **503**, 2833
 Sánchez S. F., et al., 2012, *A&A*, **538**, A8
 Sarkar S., Pandey B., Bhattacharjee S., 2021, *MNRAS*, **501**, 994
 Sellwood J. A., 2012, *ApJ*, **751**, 44
 Sellwood J. A., 2014, *Rev. Mod. Phys.*, **86**, 1
 Shen J., Zheng X.-W., 2020, *Res. Astron. Astrophys.*, **20**, 159
 Sherman S., et al., 2020, *MNRAS*, **491**, 3318
 Sheth K., et al., 2008, *ApJ*, **675**, 1141
 Skibba R. A., et al., 2012, *MNRAS*, **423**, 1485
 Smail I., et al., 2023, *ApJ*, **958**, 36
 Tremaine S., Weinberg M. D., 1984, *ApJ*, **282**, L5
 Walmsley M., et al., 2023, *MNRAS*, **526**, 4768
 Zheng Y., Shen J., 2025, *ApJ*, **979**, 60

Baldry et al. (2006), outlined in Section 2.2. This estimate is only approximate, since the MW cannot be treated identically to galaxies in redshift surveys.

Baldry et al. (2006) identified the 4th and 5th nearest neighbours among galaxies with r -band absolute magnitudes $M_r < -20$ that are within 1000 km s^{-1} of the galaxy for which $\log \Sigma$ is being measured. As no complete r -band catalogue exists for the Local Volume, we instead identify the nearest significant neighbours among galaxies with extinction-corrected absolute B -band magnitudes $M_B^c < -19$.

We use the latest version of the Catalog & Atlas of the LV galaxies (LVG; Karachentsev et al. 2013) which contains 1675 galaxies within 11 Mpc of the MW with radial velocities with respect to the centroid of the Local Group within 600 km s^{-1} . Unlike the projected distances used by Baldry et al. (2006), we adopt three-dimensional distances to nearby galaxies available in the LVG catalogue.

We identify NGC 4945 ($d_4 = 3.47 \text{ Mpc}$) and Messier 82 ($d_5 = 3.61 \text{ Mpc}$) as the 4th and 5th nearest neighbours of the MW, yielding $\log \Sigma_4 = -0.98$ and $\log \Sigma_5 = -0.91$. Following Baldry et al. (2006), we approximate the MW’s local density as $\log \Sigma = -0.94$, placing it in a low-density environment, consistent with typical definitions of voids (Baldry et al. 2006; Mouhcine et al. 2007). The LVG catalogue does not provide distance uncertainties, however, varying distance by 10–15 per cent translates to a $\lesssim 0.1 \text{ dex}$ shift in $\log \Sigma$, which does not change the classification of the MW’s environment as low-density.

This paper has been typeset from a $\text{\TeX}/\text{\LaTeX}$ file prepared by the author.

APPENDIX A: DERIVATION OF $\log \Sigma$ FOR THE MILKY WAY

To place the Milky Way in the context of the observed relationship between bar rotation rate and environment, we estimate its local environmental density, following the definition of $\log \Sigma$ from